Spacecraft Attitude and Angular Rate Tracking using Reaction Wheels and Magnetorquers [*]

Mariusz Eivind Grøtte [*] **Jan Tommy Gravdahl** [*]
Tor Arne Johansen [*] **Jesper Abildgaard Larsen** [**]
Edgard Martinez Vidal [***] **Egidijus Surma** [***]

[*] *Centre of Autonomous Marine Operations and Systems (AMOS),*
Department of Engineering Cybernetics, NTNU Norwegian University
of Science and Technology, NO-7491 Trondheim, Norway (e-mails:
{mariusz.eivind.grotte, jan.tommy.gravdahl,
tor.arne.johansen }@ntnu.no).
[**] *Department of Electronic Systems, Aalborg University, 9220 Aalborg,*
Denmark (e-mail: jal@es.aau.dk).
[***] *NanoAvionics, Mokslininku str. 2A, LT-08412 Vilnius, Lithuania*
(e-mails: {edgard.martinez, egidijus.surma}@nanoavionics.com).

Abstract: Spacecraft remote sensing applications may require slew maneuvers that prioritize small ground track errors during imaging, low power consumption and quick settling time. This paper investigates attitude control with a time-varying reference for a spacecraft model actuated by reaction wheels and magnetorquers, showing (a) an analytical solution for obtaining the required reaction wheel momentum reference in a rotational maneuver; and (b) the conditions for asymptotic convergence of attitude and angular rate tracking using a quaternion-based nonlinear control law; and (c) simulation results for a 6U CubeSat in Low-Earth-Orbit performing fixed-vector pointing and slew maneuvers. In particular, if a remote sensing spacecraft shall execute a short slew maneuver and the collection of data is not required to follow a fixed ground track, then utilizing the reference quaternion propagated from initial condition may be preferred. Based on the simulated single-axis slew maneuvers, better attitude tracking performance may be achieved when the magnetorquers are actively managing the reaction wheel momentum, but decreasing their effects in the transient period may result in quicker settling time depending on chosen error tolerances.

Keywords: aerospace; output feedback control; attitude control; angular velocity stabilization; reaction wheels; magnetic control

1. INTRODUCTION

Fixed-vector pointing and slew maneuvers normally require high control accuracy for Low-Earth-Orbit (LEO) remote sensing applications. Scanning a fixed-size Earth target while slowly rotating the spacecraft may enhance image quality by utilizing improved ground sampling distance, and retrieves important geometric and radiometric information about the target or atmosphere by varying the viewing angles (Barnsley et al., 2004). Single-axis slew maneuvers may be preferred when better image quality is required along one direction such as for push-broom or whisk-broom imagers (Vane et al., 1993).

Feedback control is widely employed for stabilizing rigid body angular motion (Outbib and Vivalda, 1994; Andriano, 1993; Aeyels and Szafranski, 1988). Depending on the global considerations for spacecraft attitude track-

ing, locally stabilizing controllers that are designed using local coordinates lead to unwinding problems and do not achieve global asymptotic stability from continuous feedback control (Bhat and Bernstein, 2000). Model-independent and model-dependent proportional-derivative (PD) control laws have been regularly employed for spacecraft attitude and angular rate tracking in practice, where latter may be generalized for a desired non-zero and constant angular rate (Wen and Kreutz-Delgado, 1991; Chunodkar and Akella, 2014; Akella et al., 2015). Passivity-based tracking of attitude and angular rates has also been explored (Kristiansen et al., 2008).

Attitude control subject to saturated control inputs and system disturbances from parameter uncertainties in spacecraft and actuators has been been studied (Boskovic et al., 2004; Yoon and Tsiotras, 2008; Slotine and Di Benedetto, 1990). In particular, the sliding mode control (SMC) has been useful in practice due to its robustness to disturbances and system noise (Crassidis and Markley, 1996; Slotine and Li, 1987). Moreover, for a slew maneuver, Ki-Seok Kim and Youdan Kim (2003) investigates using a

robust backstepping controller which may enable shorter settling time and smaller demanded torques when the control law is designed carefully.

Of particular interest in this paper is control systems design where angular rates for spacecraft are desired to be non-zero and constant. This may be utilized for spacecraft remote sensing applications that do not necessarily require optimal control in terms of minimizing the power consumption or time to reorient. This paper investigates a nonlinear spacecraft model with two types of actuators: reaction wheels and magnetorquers. Similar to (Wen and Kreutz-Delgado, 1991), a quaternion-based model-dependent controller is chosen here as the control law and the conditions for asymptotic convergence of attitude and angular velocity tracking are provided. In addition, a reaction wheel motor speed regulator and a magnetic control law for reaction wheel momentum dumping are presented. It is also shown that the latter needs an appropriate update on reaction wheel momentum reference since desired angular velocity is non-zero. Based on the framework in this paper, Kristiansen et al. (2020) studies the performance of generalized super-twisting algorithm (GSTA), a second-order SMC, for pointing and slew maneuvers.

This paper is organized as follows. Section 2 presents the kinematics and dynamics for an internally actuated spacecraft. Section 3 describes the choice of nonlinear attitude tracking control law, magnetic control law and the reaction wheel motor speed regulator. Simulation results are presented in Section 4 for a 6U CubeSat in LEO performing pointing and slew maneuvers, followed by conclusions in Section 5.

2. SPACECRAFT KINEMATICS AND DYNAMICS

2.1 Reference Frames

A coordinate frame is described by $\mathcal{F}_r : \{\mathcal{O}_r; \hat{\mathbf{x}}_r, \hat{\mathbf{y}}_r, \hat{\mathbf{z}}_r\}$, where $\mathcal{O}_r$ is the origin and $\hat{\mathbf{x}}_r, \hat{\mathbf{y}}_r, \hat{\mathbf{z}}_r$ are the dextral orthonormal unit vectors. Some of the following defined frames are illustrated in Figure 1.
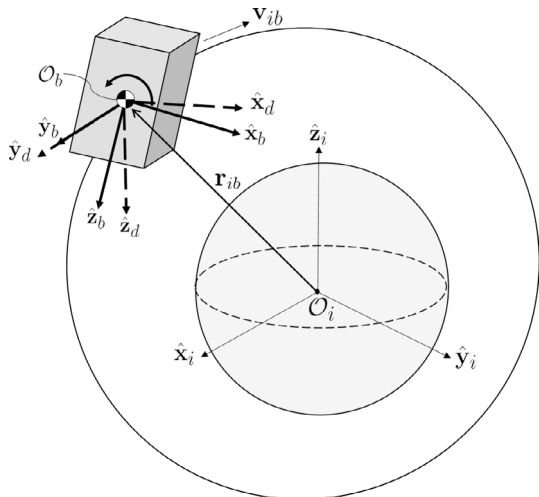

Fig. 1. Illustration of spacecraft in orbit with its defined body frame, desired frame and inertial frame.

Earth-Centered-Inertial (ECI) Frame The ECI frame $\mathcal{F}_i : \{\mathcal{O}_i; \hat{\mathbf{x}}_i, \hat{\mathbf{y}}_i, \hat{\mathbf{z}}_i\}$ represents the J2000 ECI reference located at the Earth's center of mass. The $\hat{\mathbf{x}}_i$ vector points towards the mean vernal equinox, $\hat{\mathbf{z}}_i$ points through the mean North Pole and $\hat{\mathbf{y}}_i$ is perpendicular to $\{\hat{\mathbf{x}}_i, \hat{\mathbf{z}}_i\}$.

Body Frame The body frame $\mathcal{F}_b : \{\mathcal{O}_b; \hat{\mathbf{x}}_b, \hat{\mathbf{y}}_b, \hat{\mathbf{z}}_b\}$ has origin at the spacecraft center of mass with axes along the principal axes of inertia. $\hat{\mathbf{y}}_b$ and $\hat{\mathbf{z}}_b$ point through the axes of the largest and smallest principal inertia, respectively.

Desired Frame Located at $\mathcal{O}_b$, the desired frame $\mathcal{F}_d : \{\mathcal{O}_d = \mathcal{O}_b; \hat{\mathbf{x}}_d, \hat{\mathbf{y}}_d, \hat{\mathbf{z}}_d\}$ has arbitrary chosen axes.

Orbit Frame The orbit frame $\mathcal{F}_o : \{\mathcal{O}_o = \mathcal{O}_b; \hat{\mathbf{x}}_o, \hat{\mathbf{y}}_o, \hat{\mathbf{z}}_o\}$ is defined by

$$\hat{\mathbf{z}}_o = -\frac{\mathbf{r}_{ib}}{\|\mathbf{r}_{ib}\|_2}, \hat{\mathbf{y}}_o = -\frac{\mathbf{r}_{ib} \times \mathbf{v}_{ib}}{\|\mathbf{r}_{ib} \times \mathbf{v}_{ib}\|_2}, \hat{\mathbf{x}}_o = \hat{\mathbf{y}}_o \times \hat{\mathbf{z}}_o, \quad (1)$$

where $\mathbf{r}_{ib} \in \mathbb{R}^3$ and $\mathbf{v}_{ib} \in \mathbb{R}^3$ are the spacecraft inertial position and velocity, respectively. The transformation matrix $\mathbf{R}_i^o \in \mathbb{R}^{3\times3}$ from $\mathcal{F}_i$ to $\mathcal{F}_o$, is

$$\mathbf{R}_i^o = [\hat{\mathbf{x}}_o \ \hat{\mathbf{y}}_o \ \hat{\mathbf{z}}_o]^T, \quad (2)$$

and the inertial acceleration of the spacecraft is given as

$$\mathbf{a}_{ib} = -\frac{\mu}{\|\mathbf{r}_{ib}\|_2^3}\mathbf{r}_{ib}, \quad (3)$$

with $\mu = 398600.4418 \times 10^5 \ \text{km}^3\text{s}^{-2}$ being the gravitational parameter of the Earth.

Reaction Wheel Frame The transformation from wheel frame $\mathcal{F}_w$ to body frame $\mathcal{F}_b$ is given by the matrix $\mathbf{A} \in \mathbb{R}^{n \times r} : \mathcal{F}_w \rightarrow \mathcal{F}_b$ whose column vectors $\mathbf{a}_j \in \mathbb{R}^n$ for $j = \{1, 2, \ldots, r\}$ are the spin axes of the j reaction wheels, such that

$$\mathbf{A} = [\mathbf{a}_1 \ \mathbf{a}_2 \ \cdots \ \mathbf{a}_r]. \quad (4)$$

In general, the *right* pseudo-inverse of a matrix $\mathbf{A} \in \mathbb{R}^{n \times r}$ is

$$\mathbf{A}^+ = \mathbf{A}^T \left(\mathbf{A}\mathbf{A}^T\right)^{-1}. \quad (5)$$

2.2 Kinematics

A unit-quaternion $\mathbf{q} = [\eta, \ \boldsymbol{\epsilon}]^T \in \mathbb{R}^4$ represents the rotation of $\mathcal{F}_b$ relative to $\mathcal{F}_o$, where $\eta \in \mathbb{R}$, $\boldsymbol{\epsilon} = [\epsilon_x, \ \epsilon_y, \ \epsilon_z]^T \in \mathbb{R}^3$ and the condition $\eta^2 + \boldsymbol{\epsilon}^T\boldsymbol{\epsilon} = 1$ is satisfied. The corresponding rotation matrix $\mathbf{R}_o^b \in \mathbb{R}^{3\times3}$ from $\mathcal{F}_o$ to $\mathcal{F}_b$ may be parametrized by quaternions as

$$\mathbf{R}_o^b \triangleq \mathbf{R}(\mathbf{q}) = \mathbb{I}_3 - 2\eta\mathbf{S}(\boldsymbol{\epsilon}) + \mathbf{S}(\boldsymbol{\epsilon})^2, \quad (6)$$

where $\mathbf{S}(\cdot)$ is a skew-symmetric matrix

$$\mathbf{S}(\boldsymbol{\epsilon}) = -\mathbf{S}(\boldsymbol{\epsilon})^T \triangleq \begin{bmatrix} 0 & -\epsilon_z & \epsilon_y \\ \epsilon_z & 0 & -\epsilon_x \\ -\epsilon_y & \epsilon_x & 0 \end{bmatrix}. \quad (7)$$

The kinematic differential equations may be written in compact form as

$$\dot{\mathbf{q}} = \frac{1}{2}\mathbf{T}(\mathbf{q})\boldsymbol{\omega}_{ob}^b, \quad (8)$$

where

$$\mathbf{T}(\mathbf{q}) = \begin{bmatrix} -\boldsymbol{\epsilon}^T \\ \eta\mathbb{I}_3 + \mathbf{S}(\boldsymbol{\epsilon}) \end{bmatrix}, \quad (9)$$

and $\boldsymbol{\omega}_{ob}^b \in \mathbb{R}^3$ is the angular velocity of the body frame relative to the orbit frame and expressed in body coordinates, which may also be written as

$$\boldsymbol{\omega}_{ob}^b = \boldsymbol{\omega}_{ib}^b - \mathbf{R}_o^b\boldsymbol{\omega}_{io}^o, \quad (10)$$

where

$$\boldsymbol{\omega}_{io}^o = \mathbf{R}_i^o \frac{\mathbf{S}(\mathbf{r}_{ib})\mathbf{v}_{ib}}{\|\mathbf{r}_{ib}\|_2^2}. \tag{11}$$

Additionally, the angular acceleration of the orbit frame relative to $\mathcal{F}_i$ and expressed in $\mathcal{F}_o$ is

$$\dot{\boldsymbol{\omega}}_{io}^o = \mathbf{R}_i^o \frac{\mathbf{S}(\mathbf{r}_{ib})\mathbf{a}_{ib}\mathbf{r}_{ib}^T\mathbf{r}_{ib} - 2\mathbf{S}(\mathbf{r}_{ib})\mathbf{v}_{ib}\mathbf{v}_{ib}^T\mathbf{r}_{ib}}{\|\mathbf{r}_{ib}\|_2^4}. \tag{12}$$

2.3 Nonlinear Dynamics

Considering a rigid body with internal spinning reaction wheels, the total angular momentum expressed in $\mathcal{F}_b$ is

$$\mathbf{h}^b = \mathbf{J}\boldsymbol{\omega}_{ib}^b + \mathbf{A}\mathbf{h}_s, \tag{13a}$$

where $\mathbf{J} = \mathbf{J}^T > 0 \in \mathbb{R}^{3\times 3}$ is the total system inertia matrix, $\mathbf{h}_s = \mathbf{J}_s\boldsymbol{\omega}_s \in \mathbb{R}^r$ is the axial angular momentum vector of the reaction wheels with $\mathbf{J}_s \in \mathbb{R}^{r\times r}$ being a diagonal matrix of axial reaction wheel inertia, and $\boldsymbol{\omega}_s \in \mathbb{R}^r$ being the vector of angular velocity of the reaction wheels about their respective spin axis $\mathbf{a}_j$.

Taking the time derivative of Eq. (13a), we obtain

$$\mathbf{J}\dot{\boldsymbol{\omega}}_{ib}^b = -\mathbf{S}(\boldsymbol{\omega}_{ib}^b)\mathbf{h}^b - \mathbf{A}\boldsymbol{\tau}_s + \boldsymbol{\tau}_{\text{mtq}}^b + \boldsymbol{\tau}_{\text{dist}}^b, \tag{14}$$

where $\boldsymbol{\tau}_s = \mathbf{J}_s\dot{\boldsymbol{\omega}}_s \in \mathbb{R}^r$ is vector of reaction wheel torques, $\boldsymbol{\tau}_{\text{mtq}}^b \in \mathbb{R}^3$ is the magnetic control torque and $\boldsymbol{\tau}_{\text{dist}}^b \in \mathbb{R}^3$ is the sum of environmental torques.

2.4 Disturbance Model

Environmental forces persistently perturb the spacecraft attitude and orbit (Gravdahl, 2004), where the total torque is

$$\boldsymbol{\tau}_{\text{dist}}^b = \boldsymbol{\tau}_{\text{m}}^b + \boldsymbol{\tau}_{\text{gg}}^b + \boldsymbol{\tau}_{\text{drag}}^b + \boldsymbol{\tau}_{\text{srp}}^b + \boldsymbol{\tau}_{\text{noise}}^b, \tag{15}$$

where the latter term $\boldsymbol{\tau}_{\text{noise}}^b = \mathbf{J}\delta\dot{\boldsymbol{\omega}}_{ib}^b$ may represent random disturbances from structural and thermal vibrations. The other terms are explained in detail in Markley and Crassidis (2014).

2.5 Error Dynamics

The attitude error quaternion represents the rotation of $\mathcal{F}_b$ relative to $\mathcal{F}_d$ and is defined by

$$\tilde{\mathbf{q}} = \begin{bmatrix} \tilde{\eta} \\ \tilde{\boldsymbol{\epsilon}} \end{bmatrix} = \mathbf{q}_d^{-1} \otimes \mathbf{q} = \begin{bmatrix} \eta_d\eta + \boldsymbol{\epsilon}_d^T\boldsymbol{\epsilon} \\ \eta_d\boldsymbol{\epsilon} - \eta\boldsymbol{\epsilon}_d - \mathbf{S}(\boldsymbol{\epsilon}_d)\boldsymbol{\epsilon} \end{bmatrix}, \tag{16}$$

where $\otimes$ denotes the quaternion product operator, $\mathbf{q}_d^{-1} = [\eta_d, -\boldsymbol{\epsilon}_d]^T/\|\mathbf{q}_d\|_2$ is the quaternion inverse of $\mathbf{q}_d = [\eta_d, \boldsymbol{\epsilon}_d]^T$ being the desired quaternion in reference frame $\mathcal{F}_d$ with corresponding rotation matrix $\mathbf{R}_o^d \triangleq \mathbf{R}(\mathbf{q}_d)$. Eq. (16) satisfies the condition $\tilde{\eta}^2 + \tilde{\boldsymbol{\epsilon}}^T\tilde{\boldsymbol{\epsilon}} = 1$ and the corresponding rotation matrix is

$$\mathbf{R}_d^b \triangleq \mathbf{R}(\tilde{\mathbf{q}}) = \mathbf{R}(\mathbf{q})\mathbf{R}(\mathbf{q}_d)^T = \mathbf{R}_o^b(\mathbf{R}_o^d)^T. \tag{17}$$

The kinematic differential equations of the quaternion error is

$$\dot{\tilde{\mathbf{q}}} = \frac{1}{2}\mathbf{T}(\tilde{\mathbf{q}})\tilde{\boldsymbol{\omega}}, \tag{18}$$

with two equilibria $\tilde{\mathbf{q}}_\pm = [\tilde{\eta}, \tilde{\boldsymbol{\epsilon}}]^T = [\pm 1, \mathbf{0}]^T$, and given that $\boldsymbol{\omega}_{od}^d$ is the desired angular velocity in $\mathcal{F}_d$ relative to $\mathcal{F}_o$ and expressed in $\mathcal{F}_d$, the angular velocity error is then

$$\begin{aligned} \tilde{\boldsymbol{\omega}} &= \boldsymbol{\omega}_{ob}^b - \boldsymbol{\omega}_{od}^b = \boldsymbol{\omega}_{ob}^b - \mathbf{R}_d^b\boldsymbol{\omega}_{od}^d \\ &= \boldsymbol{\omega}_{ib}^b + \mathbf{R}_o^b\boldsymbol{\omega}_{io}^o - \mathbf{R}_d^b\boldsymbol{\omega}_{id}^d - \mathbf{R}_o^b\boldsymbol{\omega}_{io}^o = \boldsymbol{\omega}_{ib}^b - \boldsymbol{\omega}_{id}^b, \tag{19} \end{aligned}$$

and the derivative with respect to $\mathcal{F}_b$ is

$$\begin{aligned} \dot{\tilde{\boldsymbol{\omega}}} &= \dot{\boldsymbol{\omega}}_{ib}^b - \mathbf{R}_d^b\dot{\boldsymbol{\omega}}_{id}^d - \dot{\mathbf{R}}_d^b\boldsymbol{\omega}_{id}^d \\ &= \dot{\boldsymbol{\omega}}_{ib}^b - \dot{\boldsymbol{\omega}}_{id}^b + \mathbf{S}(\tilde{\boldsymbol{\omega}})\boldsymbol{\omega}_{id}^b, \tag{20} \end{aligned}$$

where $\dot{\boldsymbol{\omega}}_{id}^b$ may be found from

$$\dot{\boldsymbol{\omega}}_{id}^b = \mathbf{R}_d^b\dot{\boldsymbol{\omega}}_{ob}^d + \mathbf{R}_o^b\dot{\boldsymbol{\omega}}_{io}^o - \mathbf{S}(\boldsymbol{\omega}_{od}^b)\mathbf{R}_o^b\boldsymbol{\omega}_{io}^o. \tag{21}$$

Remark 1: For trajectories in Eq. (18) with two equilibrium points $\tilde{\eta} = \pm 1$, it is important to bear in mind that the quaternion representation does not allow for globally continuous stabilizing control laws (Bhat and Bernstein, 2000).

When omitting the terms $\boldsymbol{\tau}_{\text{dist}}^b$ and $\boldsymbol{\tau}_{\text{mtq}}^b$ in Eq. (14), the error dynamics used for attitude control stability analysis is

$$\begin{aligned} \mathbf{J}\dot{\tilde{\boldsymbol{\omega}}} &= \mathbf{J}(\dot{\boldsymbol{\omega}}_{ib}^b - \dot{\boldsymbol{\omega}}_{id}^b + \mathbf{S}(\tilde{\boldsymbol{\omega}})\boldsymbol{\omega}_{id}^b) \\ &= \mathbf{J}\mathbf{S}(\tilde{\boldsymbol{\omega}})\boldsymbol{\omega}_{id}^b - \mathbf{S}(\boldsymbol{\omega}_{id}^b)\mathbf{J}\boldsymbol{\omega}_{id}^b - \mathbf{S}(\tilde{\boldsymbol{\omega}})\mathbf{J}\boldsymbol{\omega}_{id}^b \\ &\quad - \mathbf{S}(\boldsymbol{\omega}_{id}^b)\mathbf{J}\tilde{\boldsymbol{\omega}} - \mathbf{S}(\tilde{\boldsymbol{\omega}})\mathbf{J}\tilde{\boldsymbol{\omega}} - \mathbf{A}\boldsymbol{\tau}_s - \mathbf{J}\dot{\boldsymbol{\omega}}_{id}^b \\ &\quad - \mathbf{S}(\tilde{\boldsymbol{\omega}})\mathbf{A}\mathbf{J}_s\boldsymbol{\omega}_s - \mathbf{S}(\boldsymbol{\omega}_{id}^b)\mathbf{A}\mathbf{J}_s\boldsymbol{\omega}_s, \tag{22} \end{aligned}$$

where the following has been used

$$\begin{aligned} \mathbf{S}(\boldsymbol{\omega}_{ib}^b)\mathbf{J}\boldsymbol{\omega}_{ib}^b &= \mathbf{S}(\boldsymbol{\omega}_{id}^b + \tilde{\boldsymbol{\omega}})\mathbf{J}(\boldsymbol{\omega}_{id}^b + \tilde{\boldsymbol{\omega}}) \\ &= \mathbf{S}(\boldsymbol{\omega}_{id}^b)\mathbf{J}\boldsymbol{\omega}_{id}^b + \mathbf{S}(\tilde{\boldsymbol{\omega}})\mathbf{J}\boldsymbol{\omega}_{id}^b \\ &\quad + \mathbf{S}(\boldsymbol{\omega}_{id}^b)\mathbf{J}\tilde{\boldsymbol{\omega}} + \mathbf{S}(\tilde{\boldsymbol{\omega}})\mathbf{J}\tilde{\boldsymbol{\omega}}, \tag{23a} \end{aligned}$$

$$\begin{aligned} \mathbf{S}(\boldsymbol{\omega}_{ib}^b)\mathbf{A}\mathbf{J}_s\boldsymbol{\omega}_s &= \mathbf{S}(\boldsymbol{\omega}_{id}^b + \tilde{\boldsymbol{\omega}})\mathbf{A}\mathbf{J}_s\boldsymbol{\omega}_s \\ &= \mathbf{S}(\boldsymbol{\omega}_{id}^b)\mathbf{A}\mathbf{J}_s\boldsymbol{\omega}_s + \mathbf{S}(\tilde{\boldsymbol{\omega}})\mathbf{A}\mathbf{J}_s\boldsymbol{\omega}_s. \tag{23b} \end{aligned}$$

2.6 Time-Varying Quaternion Reference

In general the desired quaternion derivative with constant desired angular velocity $\boldsymbol{\omega}_{od}^d$ can be found directly from

$$\dot{\mathbf{q}}_d = \frac{1}{2}\mathbf{T}(\mathbf{q}_d)\boldsymbol{\omega}_{od}^d, \tag{24}$$

such that using the first-order Euler method yields the time-varying reference is expressed in discrete time

$$\mathbf{q}_d[k+1] = \mathbf{q}_d[k] + \dot{\mathbf{q}}_d[k]\Delta t, \tag{25}$$

where $k+1$ is the sample at time $t + \Delta t$ with $t \in \mathbb{R}$ being the time at sample k and $\Delta t \in \mathbb{R}$ is the step size. For practical reasons, the desired quaternion reference may be propagated from an arbitrary attitude state such that $\mathbf{q}_d[0] = \mathbf{q}[0]$ in Eqs. (25) and (24).

2.7 Angular Momentum Reference

For momentum management, the axial angular momentum error of reaction wheels may be defined as the difference between the desired axial angular momentum of the reaction wheels $\mathbf{h}_{s,d}$ and $\mathbf{h}_s$ such that

$$\tilde{\mathbf{h}}_s^b = \mathbf{A}\tilde{\mathbf{h}}_s = \mathbf{A}(\mathbf{h}_{s,d} - \mathbf{h}_s). \tag{26}$$

Rewriting Eq. (13a), the desired total angular momentum $\mathbf{h}_d$ expressed in $\mathcal{F}_d$ requires that

$$\mathbf{h}_d^d \triangleq \mathbf{J}\mathbf{R}_o^d\boldsymbol{\omega}_{io}^o = \mathbf{J}\boldsymbol{\omega}_{id}^d + \mathbf{A}\mathbf{h}_{s,d} \tag{27}$$

where $\mathbf{h}_{s,d} = \mathbf{J}_s\boldsymbol{\omega}_{s,d}$ and $\boldsymbol{\omega}_{s,d} \in \mathbb{R}^r$ is the reference reaction wheel speed. Thus, the reference angular momentum in $\mathcal{F}_d$ is

$$\mathbf{A}\mathbf{J}_s\boldsymbol{\omega}_{s,d} = -\mathbf{J}\boldsymbol{\omega}_{od}^d, \tag{28}$$

which is a linear system of equations and is overdetermined for $r > n$ or underdetermined for $n > r$.

We define $\boldsymbol{\omega}_{od_0}^d \triangleq \boldsymbol{\omega}_{od}^d = \mathbf{0}$ as the desired angular velocity at rest, i.e. a case where the spacecraft shall point fixed at an arbitrary chosen attitude. For a rotational maneuver from resting condition then the desired reaction wheel speed may be chosen with respect to resting condition as

$$\mathbf{AJ}_s(\boldsymbol{\omega}_{s,d} - \boldsymbol{\omega}_{s,d_0}) = -\mathbf{J}(\boldsymbol{\omega}_{od}^d - \boldsymbol{\omega}_{od_0}^d),$$
$$\Rightarrow \boldsymbol{\omega}_{s,d} = -\mathbf{J}_s^{-1}\mathbf{A}^+\mathbf{J}\boldsymbol{\omega}_{od}^d + \boldsymbol{\omega}_{s,d_0}, \qquad (29)$$

such that $\boldsymbol{\omega}_{s,d}$ is a unique minimal solution.

Example 1: Consider the configuration of three orthogonally placed reaction wheels with respect to each $\mathcal{F}_b$-axis and a fourth reaction wheel with the spin axis inclined at 54.7 deg with respect to each $\mathcal{F}_b$-axis, then the matrix $\mathbf{A}$ becomes

$$\mathbf{A} = \begin{bmatrix} 1 & 0 & 0 & \frac{1}{\sqrt{3}} \\ 0 & 1 & 0 & \frac{1}{\sqrt{3}} \\ 0 & 0 & 1 & \frac{1}{\sqrt{3}} \end{bmatrix}. \qquad (30)$$

For pointing nadir or at an arbitrary desired attitude, the spacecraft is desired to be at rest with $\boldsymbol{\omega}_{od}^d = \mathbf{0}$. By setting $\omega_{s,d_0,1} = \omega_{s,d_0,2} = \omega_{s,d_0,3}$ and $J_s = J_{s,j}$ for $j = \{1,2,3,4\}$ then, in general, there are infinitely many solutions for

$$\boldsymbol{\omega}_{s,d_0} = \begin{bmatrix} \omega_{s,d_0,1} \\ \omega_{s,d_0,2} \\ \omega_{s,d_0,3} \\ \omega_{s,d_0,4} \end{bmatrix} = \beta \begin{bmatrix} 1 \\ 1 \\ 1 \\ -\sqrt{3} \end{bmatrix}, \ \boldsymbol{\omega}_{od}^d = \boldsymbol{\omega}_{od_0}^d = \mathbf{0}, \quad (31)$$

which is parametrized by $\beta \in \mathbb{R}$ such that the net axial angular momentum of reaction wheels is $\sum_{j=1}^4 h_{s,d_0,j}^b = 0$ and Eq. (28) is satisfied.

Remark 2: The parameter β may be constrained by the upper reaction wheel speed limit such that $0 \leq \sqrt{3}|\beta| < \omega_{s,\max,j}$. Even though small values of β are theoretically a solution to Eq. (31), these are not desirable due practical limitations of brushless direct current (DC) motors running at low speeds, therefore β should be carefully chosen to maximize the mechanical efficiency of the reaction wheels and simultaneously avoid the vicinity of motor speed dead-zone and saturation.

3. CONTROLLER DESIGN

A block diagram of control systems for the spacecraft and motor dynamics is shown in Figure 2. The reaction wheel speed is controlled by a motor speed regulator using the error between commanded and actual motor speed, i.e. $\tilde{\boldsymbol{\omega}}_s \triangleq \boldsymbol{\omega}_{s,\mathrm{cmd}} - \boldsymbol{\omega}_s$. Feedback and feedforward terms are utilized in the attitude error tracking controller that requires immediate knowledge of $\boldsymbol{\omega}_s$. $\hat{\tilde{\mathbf{q}}}$ and $\hat{\tilde{\boldsymbol{\omega}}}$ denote the error state when an observer is used.

Defining the control input

$$\mathbf{u}^b \triangleq -\mathbf{A}\boldsymbol{\tau}_s, \qquad (32)$$

the relationship between the commanded torque $\boldsymbol{\tau}_{s,\mathrm{cmd}} \in \mathbb{R}^r$ and $\mathbf{u}^b$ may be expressed as

$$\boldsymbol{\tau}_{s,\mathrm{cmd}} \triangleq -\mathbf{A}^+\mathbf{u}^b, \qquad (33)$$

which maps the control input of minimum norm from $\mathcal{F}_b \to \mathcal{F}_w$ and gives the commanded motor speed $\boldsymbol{\omega}_{s,\mathrm{cmd}} \in \mathbb{R}^r$, propagated in discrete time as

$$\boldsymbol{\omega}_{s,\mathrm{cmd}}[0] = \boldsymbol{\omega}_s[0], \qquad (34a)$$
$$\boldsymbol{\omega}_{s,\mathrm{cmd}}[k+1] = \boldsymbol{\omega}_{s,\mathrm{cmd}}[k] - \mathbf{J}_s^{-1}\boldsymbol{\tau}_{s,\mathrm{cmd}}[k]\Delta t. \qquad (34b)$$

3.1 Nonlinear Controller

Proposition 1: Given a smooth continuous trajectory $\boldsymbol{\omega}_{od}^b$ that is twice differentiable for $t \geq 0$, the control law

$$\mathbf{u}^b \triangleq -k_p\mathrm{sgn}(\tilde{\eta})\tilde{\boldsymbol{\epsilon}} - k_d\tilde{\boldsymbol{\omega}} + \mathbf{S}(\boldsymbol{\omega}_{id}^b)(\mathbf{J}\boldsymbol{\omega}_{id}^b + \mathbf{AJ}_s\boldsymbol{\omega}_s)$$
$$+ \mathbf{J}\dot{\boldsymbol{\omega}}_{id}^b, \qquad (35)$$

where $k_p, k_d > 0 \in \mathbb{R}$, $\mathrm{sgn}(\tilde{\eta}) \triangleq 1$ when $\tilde{\eta} \geq 0$ and $\mathrm{sgn}(\tilde{\eta}) \triangleq -1$ when $\tilde{\eta} < 0$ for all $t \geq 0$, makes the solution trajectories of Eqs. (16) and (22) converge asymptotically to the origin such that $\tilde{\boldsymbol{\epsilon}}(t) \to \mathbf{0}$, $\tilde{\eta}(t) \to \pm 1$ and $\tilde{\boldsymbol{\omega}}(t) \to \mathbf{0}$ as $t \to \infty$ for all $\tilde{\boldsymbol{\epsilon}}(0)$, $\tilde{\eta}(0)$ and $\tilde{\boldsymbol{\omega}}(0)$. Furthermore, the origin $\mathbf{x} = \mathbf{0}$ is uniformly stable (US).

Proof: We define a Lyapunov function candidate with state $\mathbf{x} = [\tilde{\boldsymbol{\omega}}, \ 1 - |\tilde{\eta}|, \ \tilde{\boldsymbol{\epsilon}}]^T$, such that

$$V(t, \mathbf{x}) = \frac{1}{2}\tilde{\boldsymbol{\omega}}^T\mathbf{J}\tilde{\boldsymbol{\omega}} + k_p((1 - |\tilde{\eta}|)^2 + \tilde{\boldsymbol{\epsilon}}^T\tilde{\boldsymbol{\epsilon}}), \qquad (36)$$

which is positive definite for all t. The time derivative of $V(t, \mathbf{x})$ along the trajectory of the system in Eqs. (16) and (22) is

$$\dot{V} = \tilde{\boldsymbol{\omega}}^T\mathbf{J}\dot{\tilde{\boldsymbol{\omega}}} + k_p\mathrm{sgn}(\tilde{\eta})\tilde{\boldsymbol{\epsilon}}^T\tilde{\boldsymbol{\omega}}$$
$$= -\tilde{\boldsymbol{\omega}}^T\mathbf{J}\dot{\boldsymbol{\omega}}_{id}^b - \tilde{\boldsymbol{\omega}}^T[\mathbf{S}(\boldsymbol{\omega}_{id}^b)\mathbf{J} + \mathbf{JS}(\boldsymbol{\omega}_{id}^b)]\tilde{\boldsymbol{\omega}}$$
$$- \tilde{\boldsymbol{\omega}}^T\mathbf{S}(\boldsymbol{\omega}_{id}^b)\mathbf{J}\boldsymbol{\omega}_{id}^b - \tilde{\boldsymbol{\omega}}^T\mathbf{S}(\boldsymbol{\omega}_{id}^b)\mathbf{AJ}_s\boldsymbol{\omega}_s + \tilde{\boldsymbol{\omega}}^T\mathbf{u}^b$$
$$+ k_p\mathrm{sgn}(\tilde{\eta})\tilde{\boldsymbol{\epsilon}}^T\tilde{\boldsymbol{\omega}} = -k_d\tilde{\boldsymbol{\omega}}^T\tilde{\boldsymbol{\omega}} = -k_d\|\tilde{\boldsymbol{\omega}}\|_2^2 \leq 0, \qquad (37)$$

where we have used the fact that $\tilde{\boldsymbol{\omega}}^T\mathbf{S}(\tilde{\boldsymbol{\omega}}) = 0$ and $\tilde{\boldsymbol{\omega}}^T[\mathbf{JS}(\boldsymbol{\omega}_{id}^b) + \mathbf{S}(\boldsymbol{\omega}_{id}^b)\mathbf{J}]\tilde{\boldsymbol{\omega}} = 0$, and the control law defined in Eq. (35).

Integrating the inequality in Eq. (37)

$$V(t, \mathbf{x}(t)) - V(0, \mathbf{x}(0)) = \int_0^t -k_d\|\tilde{\boldsymbol{\omega}}(z)\|_2^2 dz \leq 0, \qquad (38)$$

means that $\lim_{t \to \infty} V(t, \mathbf{x}(t))$ exists and is finite and $\tilde{\boldsymbol{\omega}}(t)$ is uniformly bounded. Consequently, using Eq. (18) then $\dot{\tilde{\mathbf{q}}}(t)$ and $\tilde{\mathbf{q}}(t)$ are also uniformly bounded.

Integrating $\ddot{V}(t, \mathbf{x}(t))$

$$\dot{V}(t, \mathbf{x}(t)) - \dot{V}(0, \mathbf{x}(0)) = \int_0^t -2k_d\tilde{\boldsymbol{\omega}}(z)^T\dot{\tilde{\boldsymbol{\omega}}}(z)dz$$
$$= -k_d\|\tilde{\boldsymbol{\omega}}(t)\|_2^2 + k_d\|\tilde{\boldsymbol{\omega}}(0)\|_2^2, \qquad (39)$$

which shows that $\ddot{V}(t, \mathbf{x}(t))$ is uniformly bounded for all t. With application of Barbalat's lemma [Lemma 8.2,(Khalil, 2002)], then $\dot{V}(t, \mathbf{x}(t))$ is uniformly continuous and $\lim_{t \to \infty} \dot{V}(t, \mathbf{x}(t)) = 0$. Thus the origin $\mathbf{x} = \mathbf{0}$ is uniformly stable (US).

Since $\lim_{t \to \infty} \dot{\tilde{\boldsymbol{\omega}}}(t)$ exists and is finite then $\lim_{t \to \infty} \tilde{\boldsymbol{\omega}}(t) = \mathbf{0}$. Using Eq. (18), we have

$$\lim_{t \to \infty} \dot{\tilde{\mathbf{q}}}(t) = \frac{1}{2} \lim_{t \to \infty} [\mathbf{T}(\tilde{\mathbf{q}}(t))\tilde{\boldsymbol{\omega}}(t)], \qquad (40)$$

which implies that $\lim_{t \to \infty} \dot{\tilde{\mathbf{q}}}(t) = \mathbf{0}$. Using the fact that $\boldsymbol{\omega}_{id}^b(t)$ is twice differentiable then $\lim_{t \to \infty} \ddot{\tilde{\boldsymbol{\omega}}}(t)$ exists and is finite, thus $\lim_{t \to \infty} \dot{\tilde{\boldsymbol{\omega}}}(t) = \mathbf{0}$. With $\lim_{t \to \infty} \tilde{\boldsymbol{\omega}}(t) = \mathbf{0}$ and using Eq.(32) and Eq. (35) in Eq. (22), we have

$$\lim_{t \to \infty} \dot{\tilde{\boldsymbol{\omega}}}(t) = \lim_{t \to \infty} [\mathrm{sgn}(\tilde{\eta}(t))\tilde{\boldsymbol{\epsilon}}(t)], \qquad (41)$$
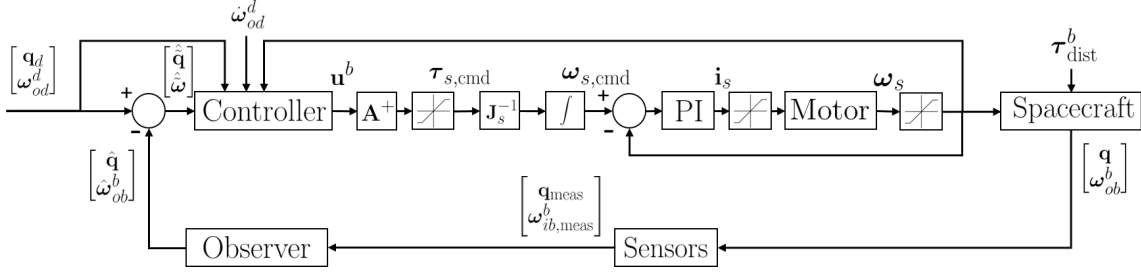
Fig. 2. Block diagram for the spacecraft and reaction wheel closed loop systems.

which implies that $\lim_{t\to\infty} \tilde{\boldsymbol{\epsilon}}(t) = \mathbf{0}$ when $\lim_{t\to\infty} \dot{\tilde{\boldsymbol{\omega}}}(t) = \mathbf{0}$. From the identity $\tilde{\eta}^2 + \tilde{\boldsymbol{\epsilon}}^T\tilde{\boldsymbol{\epsilon}} = 1$ it follows that $\lim_{t\to\infty} \tilde{\eta}(t) = 1$ when $\tilde{\eta}(t) \geq 0$ and $\lim_{t\to\infty} \tilde{\eta}(t) = -1$ when $\tilde{\eta}(t) < 0$.

3.2 Momentum Management Controller

Proposition 2: The control law
$$\boldsymbol{\tau}_{\text{mtq}}^b \triangleq -\mathbf{m}_{\text{mtq}}^b \times \mathbf{B}^b, \tag{42}$$
with the magnetic moment
$$\mathbf{m}_{\text{mtq}}^b = k_{\text{mtq}} \left(\tilde{\mathbf{h}}_s^b \times \frac{\mathbf{B}^b}{\|\mathbf{B}^b\|_2^2} \right), \tag{43}$$
where $k_{\text{mtq}} > 0 \in \mathbb{R}$ and $\mathbf{B}^b$ is the local magnetic field of the Earth expressed in body coordinates, guarantees global exponential stability of the system $\dot{\tilde{\mathbf{h}}}_s^b$. For a Pulse-Width-Modulated (PWM) signal, the voltage command $\mathbf{v}_{\text{mtq}} \in \mathbb{R}^3$ required by the magnetorquers is
$$\mathbf{v}_{\text{mtq}} = k_{\text{mv}} \mathbf{m}_{\text{mtq}}^b, \tag{44}$$
where $k_{\text{mv}} > 0 \in \mathbb{R}$ is a gain that transforms magnetic moment to demanded voltage.

Proof: The chosen control law Eqs. (42) and (43) guarantees global exponential stability in the closed-loop system $\dot{\tilde{\mathbf{h}}}_s^b = -\mathbf{B}^b \times \mathbf{m}_{\text{mtq}}^b$ as shown in (Tregouet et al., 2015).

3.3 Motor Controller

A proportional-integral (PI) controller provides the required current $i_{s,j} \in \mathbb{R}$ to regulate the reaction wheel speed
$$i_{s,j} \triangleq k_{p,\text{motor}} \tilde{\omega}_{s,j} + k_{i,\text{motor}} \int \tilde{\omega}_{s,j} dt, \tag{45}$$
where $k_{p,\text{motor}}, k_{i,\text{motor}} > 0 \in \mathbb{R}$.

Suppose the reaction wheel is driven by a brushless DC motor, then the relationship between axial torque, armature current and reaction wheel speed is expressed as
$$\tau_{s,j} = J_{s,j} \dot{\omega}_{s,j} = k_{t,j} i_{s,j} - b_{\omega_{s,j}} \omega_{s,j}, \tag{46}$$
where $k_{t,j} > 0 \in \mathbb{R}$ is the motor torque constant, $b_{\omega_{s,j}} > 0 \in \mathbb{R}$ is the motor friction coefficient which varies with reaction wheel speed.

4. NUMERICAL RESULTS

In this section, numerical results are provided for a 6U CubeSat in LEO performing fixed-vector pointing and rotational maneuvers with the control laws defined in Eqs. (35), (42) and (45). The model follows the design in Figure 2. The chosen spacecraft in the simulations is

a NanoAvionics' M6P platform and reaction wheels are based on 4RW0 specifications mounted as defined in Eq. (30). The system inertia matrix and the axial reaction wheel inertia matrix are
$$\mathbf{J} = \begin{bmatrix} J_{xx} & J_{xy} & J_{xz} \\ J_{yx} & J_{yy} & J_{yz} \\ J_{zx} & J_{zy} & J_{zz} \end{bmatrix}, \quad \mathbf{J}_s = J_s \mathbb{I}_4, \tag{47}$$
where $J_s = J_{s,j}$ for $j = \{1, 2, 3, 4\}$ is the axial inertia of a single reaction wheel and are identical. Also, three magnetorquers are placed separately along each body axis.

The orbit parameters are provided in Table 1 while physical parameters and control gains are shown in Tables 2 and 3, respectively. The sampling rate is set at $\Delta t = 4$ Hz. The voltage to reaction wheels $v_s = v_{s,j}$ for $j = \{1, 2, 3, 4\}$ and resistance of each magnetorquer coil R_{mtq} are treated as constant. The term $\boldsymbol{\tau}_{\text{noise}}^b$ in Eq. (15) is modeled with random noise $\delta\dot{\boldsymbol{\omega}}_{ib}^b \sim \mathcal{N}\left(0, 4.9 \times 10^{-11}\right)$ deg $\cdot$ s^{-2}. The other terms in $\boldsymbol{\tau}_{\text{dist}}^b$ are modeled based on (Markley and Crassidis, 2014), where S_j for $j = \{1, 2, 3, 4, 5, 6\}$ denote the six surface areas of the spacecraft, $c_{\text{diff}} = c_{\text{diff},j}$ and $c_{\text{refl}} = c_{\text{refl},j}$ for $j = \{1, 2, 3, 4, 5, 6\}$ are the Lambertian diffuse reflection coefficient and specular reflection coefficient of the jth plate, respectively. $\mathbf{r}_{cp,j}^b$ is the center of pressure position on the jth plate, C_d is the drag coefficient and $\mathbf{m}_{\text{res}}^b$ is the residual magnetic moment. The IGRF-12 model is used to simulate the Earth's magnetic field.

Furthermore, reaction wheel jitter effects are modeled with $\delta\omega_{s,j} \sim \mathcal{N}(0, 4)$ rpm, while saturation limits are set to $|i_j| \leq 0.6$ A, $|\omega_{s,j}| \leq 6500$ rpm, $|\dot{\omega}_{s,j}| \leq 4.5 \times 10^{-3}$ rad $\cdot$ s^{-2}, $|\tau_{s,j}| \leq 3.2 \times 10^{-3}$ Nm and $|h_{s,j}| \leq 20 \times 10^{-3}$ Nms. The resolution of reaction wheel speed is set to 0.1 rpm and the speed dead-zone is $\omega_{s,j} = 0$ if $|\omega_{s,j}| \leq 100$ rpm. The magnetorquers moment saturates at $|m_l^b| \leq 0.93$ Am^2 along each axis $l = \{x, y, z\}$.

We may express the spacecraft attitude, desired attitude and attitude error with Euler angles, i.e. $\boldsymbol{\Phi} = [\phi, \theta, \psi]^T$, $\boldsymbol{\Phi}_d = [\phi_d, \theta_d, \psi_d]^T$ and $\tilde{\boldsymbol{\Phi}} = \boldsymbol{\Phi} - \boldsymbol{\Phi}_d$. Although observer design is beyond the scope of this paper, the results are presented with simulated observer output $\hat{\boldsymbol{\Phi}} = \boldsymbol{\Phi} + \delta\hat{\boldsymbol{\Phi}}$ where the observer error is assumed to be normally distributed such that $\delta\hat{\boldsymbol{\Phi}} \sim \mathcal{N}\left(\beta_{\hat{\boldsymbol{\Phi}}}, \sigma_{\hat{\boldsymbol{\Phi}}}^2\right)$ with $\beta_{\hat{\boldsymbol{\Phi}}} = 3.4 \times 10^{-3}$ deg being the static bias and $\sigma_{\hat{\boldsymbol{\Phi}}} = 5.2 \times 10^{-3}$ deg being the standard deviation. Likewise, for $\hat{\boldsymbol{\omega}}_{ib}^b = \boldsymbol{\omega}_{ib}^b + \delta\hat{\boldsymbol{\omega}}_{ib}^b$ we have $\delta\hat{\boldsymbol{\omega}}_{ib}^b \sim \mathcal{N}\left(\beta_{\hat{\boldsymbol{\omega}}_{ib}^b}, \sigma_{\hat{\boldsymbol{\omega}}_{ib}^b}^2\right)$ with $\beta_{\hat{\boldsymbol{\omega}}_{ib}^b} = 1.32 \times 10^{-6}$ deg $\cdot$ s^{-1} and $\sigma_{\hat{\boldsymbol{\omega}}_{ib}^b} = 8 \times 10^{-3}$ deg $\cdot$ s^{-1}. In this

simulation, the error states are redefined as $\hat{\tilde{\mathbf{q}}} = \mathbf{q}_d^{-1} \otimes \hat{\mathbf{q}}$ and $\hat{\tilde{\boldsymbol{\omega}}} = \hat{\boldsymbol{\omega}}_{ob}^b - \boldsymbol{\omega}_{od}^b$ with corresponding rotation matrix $\hat{\mathbf{R}}_d^b = \hat{\mathbf{R}}_o^b (\mathbf{R}_o^d)^T$.

Table 1. Orbital parameters

Orbital element	Value
Simulation Start Time	1 July 2019 11:30:00
Semi-major axis	6871.2 km
Eccentricity	0.005
Inclination	97.6 deg
Right ascension of the ascending node	80 deg
Argument of periapsis	0 deg
True anomaly at epoch	0 deg

Table 2. Physical parameters

Physical parameter	Value
J_{xx}	7.75×10^{-2} kgm^2
$J_{xy} = J_{yx}$	2×10^{-4} kgm^2
J_{yy}	1.067×10^{-1} kgm^2
$J_{yz} = J_{zy}$	5×10^{-4} kgm^2
J_{zz}	3.89×10^{-2} kgm^2
$J_{zx} = J_{xz}$	-2×10^{-4} kgm^2
J_s	2.2984×10^{-4} kgm^2
$S_1 = S_5$	0.03 m^2
$S_2 = S_4$	0.06 m^2
$S_3 = S_6$	0.02 m^2
C_d	2
c_{diff}	0.244
c_{refl}	0.2
$\mathbf{m}_{\text{res}}^b$	$0.0125[-0.5/\sqrt{3}\ 1.4/\sqrt{3}\ -2.5/\sqrt{3}]^T$ Am^2
$\mathbf{r}_{cp,1}^b$	$[0.1009\ 0.0004\ 0.0633]^T$ m
$\mathbf{r}_{cp,2}^b$	$[-0.0991\ 0.0004\ 0.0633]^T$ m
$\mathbf{r}_{cp,3}^b$	$[-0.0001\ 0.0494\ 0.0633]^T$ m
$\mathbf{r}_{cp,4}^b$	$[-0.0001\ -0.0506\ 0.0633]^T$ m
$\mathbf{r}_{cp,5}^b$	$[-0.0001\ 0.0004\ 0.1933]^T$ m
$\mathbf{r}_{cp,6}^b$	$[0.0019\ -0.0016\ -0.1067]^T$ m
$K_{t,j}$	5.88×10^{-3} NmA^{-1}
$b_{\omega_{s,j}}$	6×10^{-7} Nms$\cdot$rad^{-1}
v_s	5 V
R_{mtq}	26.1 Ω

Table 3. Controller gains

Controller gain	Value
k_p	0.047538 Nm
k_d	0.053295 Nms
$k_{p,\text{motor}}$	0.017 As
$k_{i,\text{motor}}$	0.055 A
k_m	0.52 AmN^{-1}s^{-1}
k_{mv}	1.0785 VA^{-1}m^{-2}

Initial conditions are chosen as $\boldsymbol{\Phi}[0] = [-1, 33, -1]^T$ deg, $\boldsymbol{\omega}_{ob}^b[0] = [0, 0, 0]^T$ deg$\cdot$s^{-1}, and reaction wheels are set at $\boldsymbol{\omega}_s[0] = \boldsymbol{\omega}_{s,d_0}[0] = 2000\,[1, 1, 1, -\sqrt{3}]^T$ rpm. The desired attitude is $\boldsymbol{\Phi}_d[0] = [0, 30, 0]^T$ deg with corresponding quaternions propagated using Eq. (24) and (25), and the desired angular velocity is chosen as $\boldsymbol{\omega}_{od}^d = [0, -0.8, 0]^T$ deg$\cdot$s^{-1} such that the spacecraft shall only slew about its $\hat{\mathbf{y}}_b$-axis. Furthermore, setting $\dot{\boldsymbol{\omega}}_{od}^d = [0, 0, 0]^T$ deg$\cdot$s^{-2}, then $\dot{\boldsymbol{\omega}}_{id}^b$ may be found using Eq. (21). Immediate knowledge of $\boldsymbol{\omega}_s$ is assumed for the control law in Eq. (35). Figure 3 shows the attitude and angular

velocity of the spacecraft, where the system quickly follows the time-varying trajectory. Motor speeds and generated torque from all four reaction wheels that receive commanded inputs $\boldsymbol{\omega}_{s,\text{cmd}}$ are shown in Figure 4, indicating that the updated reference reaction wheel speed is tracked well and does not increase due to disturbances. Reaction wheel momentum error $\tilde{\mathbf{h}}_s^b$ for updated reference speed using Eq. (29) and the required magnetic moment $\mathbf{m}_{\text{mtq}}^b$ are shown in Figure 5. Total disturbance torque $\boldsymbol{\tau}_{\text{dist}}^b$ and rotational kinetic energy T_{rot} are shown in Figure 6. Figure 7 shows the resulting ground track error with respect to $\mathcal{F}_d$ when the $\hat{\mathbf{z}}_d$- and $\hat{\mathbf{z}}_b$-axes are projected on the Earth.

The performance of six different strategies are compared in Table 4 where initial conditions for all cases are defined as before and the actual attitude error $\tilde{\boldsymbol{\Phi}}$ and angular velocity error $\tilde{\boldsymbol{\omega}}$ are considered. Pointing A and B represent pointing control with the desired states $\boldsymbol{\Phi}_d = [0, 30, 0]^T$ deg and $\boldsymbol{\omega}_{od}^d = [0, 0, 0]^T$ deg $\cdot$ s^{-1}. Slew 1 represents a controlled rotational maneuver with the desired states $\boldsymbol{\Phi}_d[0] = [0, 30, 0]^T$ deg and $\boldsymbol{\omega}_{od}^d = [0, -0.8, 0]^T$ deg$\cdot$s^{-1}, Slew 2 represents the same as Slew 1 except for the desired quaternion is set to $\mathbf{q}_d[0] = \mathbf{q}[0]$. Letters A and B denote when magnetorquers are turned on and off, respectively. For all cases, the error tolerances are set to $|\tilde{\boldsymbol{\Phi}}| = 0.09$ deg and $|\tilde{\boldsymbol{\omega}}| = 0.08$ deg $\cdot$ s^{-1}, where $\tilde{\boldsymbol{\Phi}}$ and $\tilde{\boldsymbol{\omega}}$ are considered stationary if values remain within the given error band. The settling time (ST) for $\tilde{\boldsymbol{\Phi}}$ and $\tilde{\boldsymbol{\omega}}$, the root-mean-square (RMS) of stationary values for $\|\tilde{\boldsymbol{\Phi}}(t)\|_2$ and $\|\tilde{\boldsymbol{\omega}}(t)\|_2$, average of $\|\tilde{\mathbf{h}}_s(t)\|_2$ as well as the average of total actuator power consumption $P(t)$ are identified for all six cases. Figure 8 compares the attitude tracking performance for the Slew 1A, Slew 2A and Pointing A cases. All cases are simulated with identical noise parameters.

It can be inferred from Table 4 and Figure 8 that Slew 1 has better performance than combining Pointing A and Slew 2 in order. If a quasi-resting spacecraft shall perform a short slew maneuver and is not constrained to follow a fixed Earth ground track, then Slew 2 is the better strategy. This may be practically useful for single-axis slew maneuvers when the spacecraft body axes are initially almost aligned with the desired starting attitude of the maneuver. Also, by turning the magnetorquers off, the peaks in attitude and angular velocity responses are slightly lower and settling times are marginally improved as seen in Figure 9. In the non-transient period, having the magnetorquers turned on reduces the attitude tracking error for all cases.

5. CONCLUSIONS

Pointing and slew maneuver strategies have been investigated in this paper for an internally actuated spacecraft using a combination of quaternion-based nonlinear control law, motor speed regulation and magnetorquers for reaction wheel momentum management. In this paper we have shown that, during a single-axis slew maneuver, using updated reaction wheel momentum reference as input to the magnetic control law provides the desired robustness to external disturbances and may result in better performance in attitude tracking. In the case where a spacecraft is at quasi-resting state and shall execute a short slew ma-

Table 4. Performance of selected strategies (simulation time: $100\ s$).

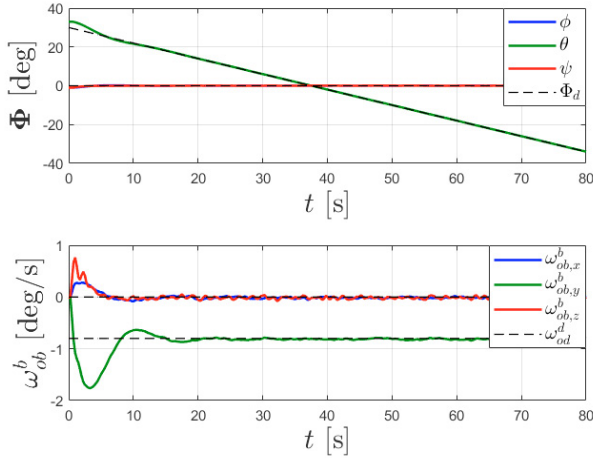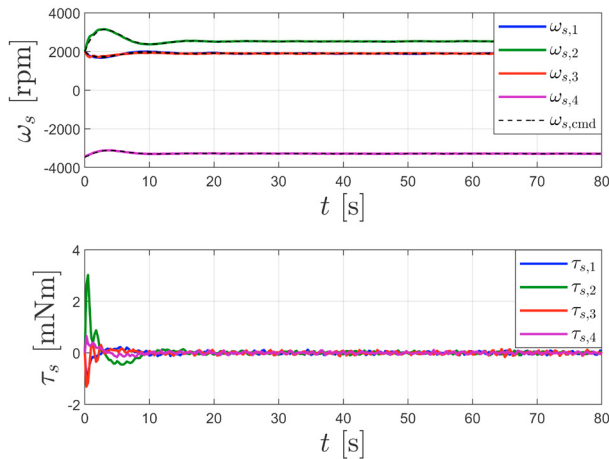| Strategy	RMS($\|\tilde{\boldsymbol{\Phi}}(t)\|_2$) [deg]	ST$_{\tilde{\Phi}}$ (s)	RMS($\|\tilde{\boldsymbol{\omega}}(t)\|_2$) [deg$\cdot$s^{-1}]	ST$_{\tilde{\omega}}$ (s)	avg($\|\tilde{\mathbf{h}}_s(t)\|_2$) [mNms]	avg($P(t)$) [W]
Pointing 1A	5.400×10^{-2}	16.50	3.739×10^{-2}	32.25	0.144	0.574
Pointing 1B	5.454×10^{-2}	15.75	3.757×10^{-2}	32.25	0.177	0.542
Slew 1A	5.800×10^{-2}	17.25	4.204×10^{-2}	12.75	0.169	0.597
Slew 1B	6.102×10^{-2}	16.50	3.966×10^{-2}	12.50	0.185	0.564
Slew 2A	5.843×10^{-2}	11.00	4.236×10^{-2}	8.25	0.091	0.549
Slew 2B	5.947×10^{-2}	11.00	3.828×10^{-2}	8.25	0.112	0.521

Fig. 3. Attitude and angular velocity vs. time.

Fig. 4. Reaction wheel speed and torque vs. time.

Fig. 5. Reaction wheel angular momentum error and magnetorquer moment vs. time.
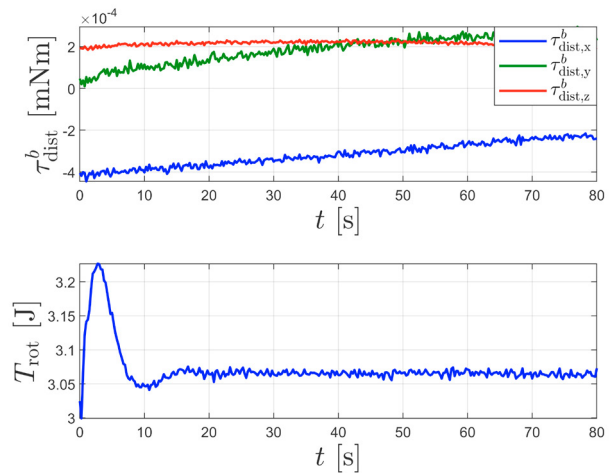
Fig. 6. Disturbance torque and rotational kinetic energy vs. time.

neuver while not constrained to follow a fixed ground track with its sensing axis, the quaternion reference should be propagated from initial condition to improve the settling time in attitude tracking. Additionally, if the risk of reaction wheel saturation is low, the magnetorquer effects may be reduced during the transient period of attitude control to improve settling time and avoid unnecessary power consumption. Future work may investigate strategies for momentum dumping and combining suitable control laws and observers with time delay effects which may be critical for mission utility in remote sensing applications.

REFERENCES

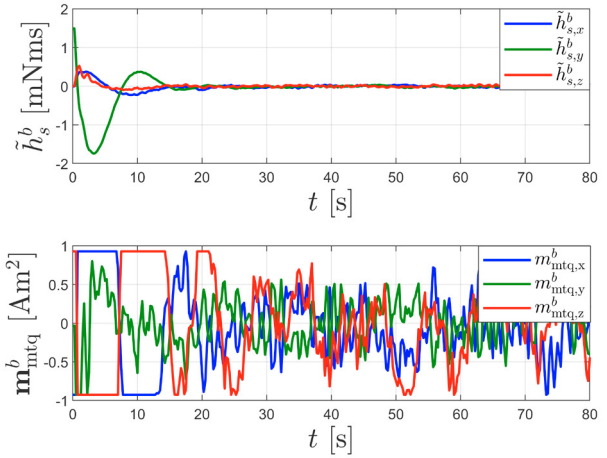Aeyels, D. and Szafranski, M. (1988). Comments on the stabilizability of the angular velocity of a rigid body. *Systems & Control Letters*, 10(1), 35 – 39.

Akella, M.R., Thakur, D., and Mazenc, F. (2015). Partial lyapunov strictification: Smooth angular velocity observers for attitude tracking control. *Journal of Guidance, Control, and Dynamics*, 38(3), 442–451.

Andriano, V. (1993). Global feedback stabilization of the angular velocity of a symmetric rigid body. *Systems & Control Letters*, 20(5), 361 – 364.

Barnsley, M.J., Settle, J.J., Cutter, M.A., Lobb, D.R., and Teston, F. (2004). The PROBA/CHRIS mission: a low-cost smallsat for hyperspectral multiangle observations of the Earth surface and atmosphere. *IEEE Transactions on Geoscience and Remote Sensing*, 42(7), 1512–
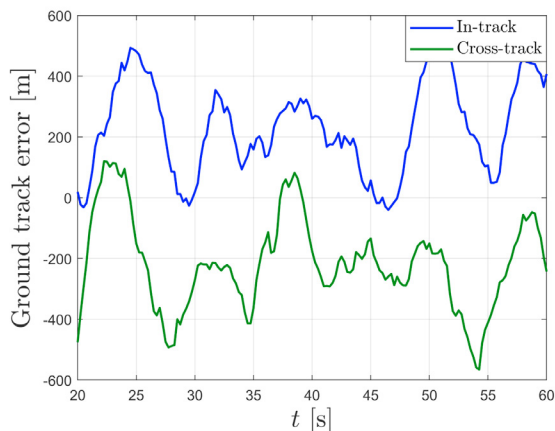
Fig. 7. Ground track error relative to $\mathcal{F}_d$ vs. time from approximately 500 km altitude. Earth curvature is neglected in this short simulation period.
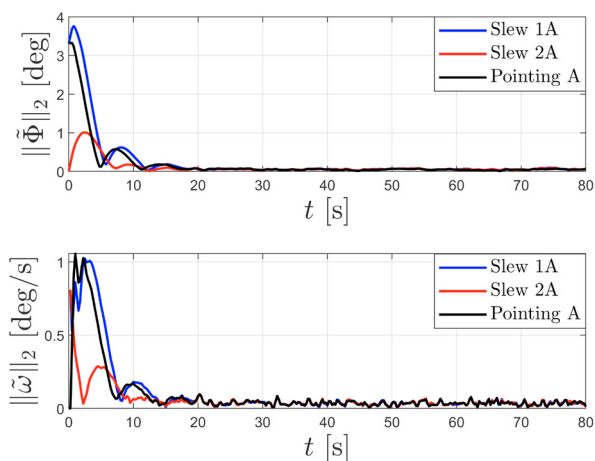

Fig. 8. Attitude and angular velocity tracking performance vs. time for Slew 1A, Slew 2A and Pointing A.
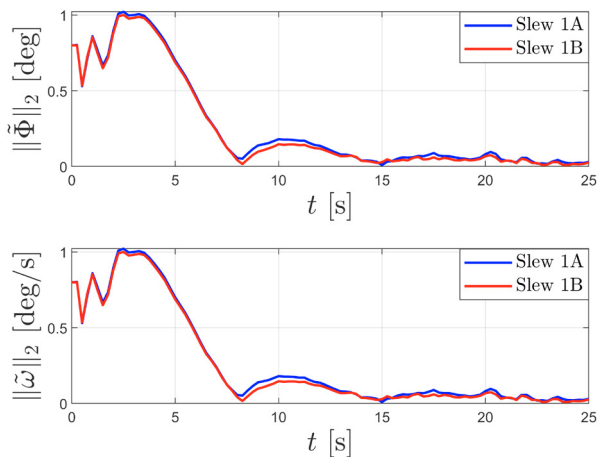

Fig. 9. Transient attitude and angular velocity tracking performance vs. time for Slew 1A, Slew 1B.

1520.

Bhat, S.P. and Bernstein, D.S. (2000). A topological obstruction to continuous global stabilization of rotational motion and the unwinding phenomenon. *Systems & Control Letters*, 39(1), 63–70.

Boskovic, J.D., Li, S.M., and Mehra, R.K. (2004). Robust tracking control design for spacecraft under control input saturation. *Journal of Guidance, Control, and Dynamics*, 27(4), 627–633.

Chunodkar, A.A. and Akella, M.R. (2014). Switching angular velocity observer for rigid-body attitude stabilization and tracking control. *Journal of Guidance, Control, and Dynamics*, 37(3), 869–878.

Crassidis, J.L. and Markley, F.L. (1996). Sliding mode control using modified rodrigues parameters. *Journal of Guidance, Control, and Dynamics*, 19(6), 1381–1383.

Gravdahl, J.T. (2004). Magnetic attitude control for satellites. In *43rd IEEE Conference on Decision and Control (CDC)*, volume 1, 261–266.

Khalil, H.K. (2002). *Nonlinear systems; 3rd ed.* Prentice-Hall, Upper Saddle River, NJ.

Ki-Seok Kim and Youdan Kim (2003). Robust backstepping control for slew maneuver using nonlinear tracking function. *IEEE Transactions on Control Systems Technology*, 11(6), 822–829.

Kristiansen, B.A., Grøtte, M.E., and Gravdahl, J.T. (2020). Quaternion-Based Generalized Super-Twisting Algorithm for Spacecraft Attitude Control. In *Proc. of the 2020 IFAC World Congress*.

Kristiansen, R., Nicklasson, P.J., and Gravdahl, J.T. (2008). Spacecraft coordination control in 6dof: Integrator backstepping vs passivity-based control. *Automatica*, 44(11), 2896 – 2901.

Markley, F.L. and Crassidis, J.L. (2014). *Fundamentals of spacecraft attitude determination and control*. Space Technology Library. Springer, New York, NY.

Outbib, R. and Vivalda, J. (1994). Stabilization of the angular velocity of the rigid body about the middle axis. *Applied Mathematics Letters*, 7(2), 45 – 48.

Slotine, J. and Di Benedetto, M.D. (1990). Hamiltonian adaptive control of spacecraft. *IEEE Transactions on Automatic Control*, 35(7), 848–852.

Slotine, J.J.E. and Li, W. (1987). On the adaptive control of robot manipulators. *The International Journal of Robotics Research*, 6(3), 49–59.

Tregouet, J.F., Arzelier, D., Peaucelle, D., Pittet, C., and Zaccarian, L. (2015). Reaction Wheels Desaturation Using Magnetorquers and Static Input Allocation. *IEEE Transactions on Control Systems Technology*, 23(2), 525 – 539.

Vane, G., Green, R.O., Chrien, T.G., Enmark, H.T., Hansen, E.G., and Porter, W.M. (1993). The airborne visible/infrared imaging spectrometer (AVIRIS). *Remote Sensing of Environment*, 44(2), 127 – 143.

Wen, J.T. and Kreutz-Delgado, K. (1991). The attitude control problem. *IEEE Transactions on Automatic Control*, 36(10), 1148–1162.

Yoon, H. and Tsiotras, P. (2008). Adaptive spacecraft attitude tracking control with actuator uncertainties. *The Journal of the Astronautical Sciences*, 56(2), 251–268.